Bioorganic Chemistry 147 (2024) 107418

Contents lists available at ScienceDirect

Bioorganic Chemistry

journal homepage: www.elsevier.com/locate/bioorg

Photocatalytic regeneration of nicotinamide cofactor biomimetics drives biocatalytic reduction by Old Yellow enzymes

Feifan Luo, Xiangyuan Gu, Yichun Zhu, Jieyu Zhou *, Guochao Xu, Ye Ni *

Key Laboratory of Industrial Biotechnology, Ministry of Education, School of Biotechnology, Jiangnan University, Wuxi 214122, Jiangsu, China

ARTICLE INFO

Keywords:
Photocatalysis
g-C_3N_4
Cofactor regeneration
Nicotinamide cofactor biomimetics
Old Yellow Enzymes

ABSTRACT

A key approach in developing green chemistry involves converting solar energy into chemical energy of biomolecules through photocatalysis. Photocatalysis can facilitate the regeneration of nicotinamide cofactors during redox processes. Nicotinamide cofactor biomimetics (NCBs) are economical substitutes for natural cofactors. Here, photocatalytic regeneration of NADH and reduced NCBs ($NCBs_{red}$) using graphitic carbon nitride (g-C_3N_4) was developed. The process involves g-C_3N_4 as the photocatalyst, Cp*Rh(bpy)H_2O^{2+} as the electron mediator, and Triethanolamine as the electron donor, facilitating the reduction of NAD^+ and various oxidative NCBs ($NCBs_{ox}$) under light irradiation. Notably, the highest reduction yield of 48.32 % was achieved with $BANA^+$, outperforming the natural cofactor NAD^+. Electrochemical analysis reveals that the reduction efficiency and capacity of cofactors relies on their redox potentials. Additionally, a coupled photo-enzymatic catalysis system was explored for the reduction of 4-Ketoisophorone by Old Yellow Enzyme XenA. Among all the $NCBs_{ox}$ and NAD^+, the highest conversion ratio of over 99 % was obtained with $BANA^+$. After recycled for 8 times, g-C_3N_4 maintained over 93.6 % catalytic efficiency. The photocatalytic cofactor regeneration showcases its outstanding performance with NAD^+ as well as $NCBs_{ox}$. This work significantly advances the development of photocatalytic cofactor regeneration for artificial cofactors and its potential application.

1. Introduction

Oxidoreductases have broad applications in industrial synthesis of various chemicals, encompassing enzymatic preparation of sugar alcohols [1], reduction of amines to produce α-amino acids by amino acid dehydrogenases [2], etc. Compared with chemical methods, enzyme-catalyzed synthesis provides benefits such as gentle reaction conditions, high catalytic efficiency, and precise stereo-/regio- specificity. Despite aforementioned merits, enzymatic redox reactions come with a significant challenge in applications. Nicotinamide cofactors NAD(P)H/$NAD(P)^+$ which consumed in enzymatic redox reactions are in high demand across the majority of industrial processes especially cell-free bioprocesses. However, substantial cost is associated with the production of unstable natural cofactors. Thus, imperative pursuit of cofactor regeneration is crucial for the practical application of oxidoreductases. Various means for cofactor recycling have been developed, including homogeneous catalysis [3], heterogeneous catalysis [4], electrochemical approaches [5], photochemical techniques [6], and enzymatic methods [7].

Enzymatic cofactor recycling remains a preferable choice in large-scale applications, due to its mild reaction conditions and high catalytic efficiency. However, addition of extra enzymes and co-substrates for cofactor regeneration also leads to production of byproducts, which complicates subsequent product recovery [8]. In photochemical methods, artificially synthesized chemical catalysts are adopted to absorb light energy for cofactor regeneration, eliminating the necessity for additional enzyme reactions. Additionally, the photochemical catalysts used in the reaction can be easily separated and recycled, representing a cost-effective and environmentally friendly option compared with other methods [9]. Various types of photocatalysts have been reported for cofactor regeneration. For example, an artificial photosynthetic system was constructed based on porphyrin. Porphyrin acts as a photosensitizer, attached to SiO_2 microspheres coated with polydopamine and polyethyleneimine containing thiol groups. Under optimal conditions, 81.5 % cofactor regeneration yield was achieved using this artificial photosynthetic system after 60 min reaction [10]. The photocatalytic antenna-reactor system, utilizing gold-rhodium nanoflowers (Au@Rh NFs), efficiency by introducing favorable electrostatic

* Corresponding authors.
E-mail addresses: zhoujieyu@jiangnan.edu.cn (J. Zhou), yni@jiangnan.edu.cn (Y. Ni).

https://doi.org/10.1016/j.bioorg.2024.107418
Received 12 March 2024; Received in revised form 17 April 2024; Accepted 28 April 2024
Available online 29 April 2024

interactions in enhance electron transfer. Using this system, the photocatalytic regeneration yield of NADH reached 30 % [11]. Another approach involves preparation of carbon nanodot-SiO_2 hybrid photocatalyst through a reverse microemulsion method using non-ionic surfactants. The cofactor regeneration yield of 74 % was reached in a photocatalyst-biocatalyst coupled system [12]. Additionally, non-metallic polymer semiconductor materials such as g-C_3N_4 have received considerable attentions in photocatalysis due to their excellent stability and favorable band edge positions. Meng et al. used g-C_3N_4 to regenerate NADH, the yield of NADH reached 27.8 % in 30 min [13]. Although the efficiency of NADH regeneration in the g-C_3N_4 system could be comparatively lower than that of other photocatalytic systems, its intrinsic characteristics, such as non-toxicity, cost-effective synthesis, high stability in acidic/alkaline environments, and responsiveness to visible light, position it as a promising photocatalyst.

The progress of photocatalytic reactions requires not only photocatalysts, but also electron mediators (EM) that transfer photoexcited electrons and electron sacrificial agents to fill photoexcited holes. The strong functionality of organometallic complex Cp*Rh(bpy)H_2O^{2+} makes it an excellent EM [14]. It exhibits high stability and activity under different reaction conditions (wide pH and temperature range), and is highly active to nicotinamide cofactors. Besides this, it exhibits high universality toward a variety of reducing equivalents, which enables it to capture photo-excited electrons from various photocatalysts. In addition, there are many options for electronic sacrificial agents, among which triethanolamine (TEOA) is widely used due to its economic and efficient characteristics. TEOA can produce photoinduced homeostasis of RO-COOH followed by a hydrogen atom transfer (HAT) process under UV light irradiation, which can interfere with the photocatalytic reaction. It is however a preferable choice in photocatalytic reactions without the use of UV light [15].

Compared with mild enzymatic regeneration reaction conditions, photocatalytic regeneration may pose challenges to the stability of cofactors. Synthetic nicotinamide cofactors have substantial potential for economical and biorthogonal cofactor regeneration compared with costly and delicate natural cofactors, owing to their robustness and easy preparation [16]. In recent years, NCBs have been demonstrated as promising substitutes for natural cofactors in redox catalysis. Seiber et al. synthesized a simple nicotinamide cofactor mimic P2NAH, retaining the nicotinamide moiety but replacing the remaining part with a single phenylpropyl. Enoate reductase (*Ts*ER, from *Thermus scotoductus*) and glucose dehydrogenase (*Ss*GDH, from *Sulfolobus solfataricus*) could utilize the biomimetic P2NAH as a cofactor to produce 2-methylbutanal, demonstrating it is applicable in enzymatic reactions [17]. Additionally, NCBs have been demonstrated to serve as redox intermediate in reactions catalyzed by OYE [18]. By utilizing NCBs, OYE can catalyze the reduction of α, β-unsaturated carbonyl compounds.

Here, a photocatalytic system mediated by g-C_3N_4 was constructed for the regeneration of NAD^+ and four distinct $NCBs_{ox}$. In this cofactor regeneration system, the semiconductor g-C_3N_4 served as a photocatalyst, being photoexcited to generate photoelectrons. TEOA acted as the sacrificial electron donor, supplying electrons to the entire reaction system. Cp*Rh(bpy)H_2O^{2+} functioned as EM, absorbing electrons from the photocatalyst and selectively catalyzing the reduction of NAD^+ and $NCBs_{ox}$. The regeneration efficiency among NCBs and natural cofactor were evaluated in terms of yield, total turnover number (TTN) and turnover frequency (TOF), etc. Furthermore, the feasibility of photocatalytic cofactor regeneration was validated by coupling with OYE (XenA from *Pseudomonas putida*) catalyzed reduction of 4-Ketoisophorone, and was also evaluated in terms of yield, TTN_{XenA}, and TOF_{XenA}.

2. Experimental section

2.1. Chemicals

Urea, triethanolamine, sodium phosphate monobasic monohydrate, sodium phosphate dibasic heptahydrate, ethyl acetate, CH_2Cl_2, acetonitrile were purchased from China National Medicines Corporation Ltd. Cp*Rh(bpy)H_2O^{2+}, β-nicotinamide adenine dinucleotide hydrate, 4-Ketoisophorone, benzyl bromide, 1, 4-dioxane, (4-bromomethyl) benzoic acid, (3-bromopropyl) benzene, diethyl ether were purchased from Sigma-Aldrich (St. Louis, MO, USA). These chemicals were used without further purification.

2.2. The preparation of g-C_3N_4

A high-temperature heating process involving carbon and nitrogen-rich precursors was employed [19]. Specifically, 10 g of urea were enclosed in a covered porcelain crucible, sealed entirely with tin foil. The crucible was placed in a muffle furnace, and the temperature was increased to 550 ℃ over 2 h, with a heating rate of 5 ℃ min^{-1}. After reaching the desired temperature, the muffle furnace was left to cool naturally to 200 ℃. A total of 0.44 g of the product was yielded.

2.3. The synthesis of nicotinamide biomimetics

Oxidative forms of four NCBs were synthesized following established literature procedures. **BNA^+ [20]:** Nicotinamide (15 mM) dissolved in 1, 4-dioxane (50 mL)/ methanol (25 mL), with the addition of 7 mM benzyl bromide, underwent reflux for 6 h. The resulting solution was filtered, and the solid product was purified by washing with CH_2Cl_2 and hexanes. **$BANA^+$ [21]:** Nicotinamide (15 mM) dissolved in 1, 4-dioxane (50 mL)/ methanol (25 mL), with the addition of 7 mM (4-bromomethyl) benzoic acid, underwent reflux for 6 h. The resulting solution was filtered, and the solid product was purified by washing with CH_2Cl_2 and hexanes. **$P2NA^+$ [17]:** Nicotinamide (40 mM) in 40 mL acetonitrile was refluxed, and 40 mM (2-chloroethyl) benzene was added, followed by stirring under reflux for 115 h. After cooling, 50 mL diethyl ether was added, and the precipitate was filtered and washed twice with diethyl ether. The product was purified using soxhlet extraction with ethyl acetate. **$P3NA^+$ [17]:** Nicotinamide (40 mM) in 50 mL acetonitrile was refluxed, and 40 mM (3-bromopropyl) benzene was added, followed by stirring under reflux for 67 h. After cooling, 50 mL diethyl ether was added, and the precipitate was filtered and washed twice with diethyl ether.

2.4. Characterization of g-C_3N_4

The morphological characteristics of g-C_3N_4 were assessed using a JEM-2100 plus transmission electron microscope (JEOL, Japan) at 200 kV and a SU8220 Cold Field Emission Scanning Electron Microscope (Hitachi, Japan). Raman spectroscopy was conducted with a LabRAM HR Evolution (Horiba Jobin Yvon Inc., France) using 532 nm laser excitation, a 300 gr min^{-1} grid tray, and a 1 s acquisition time. The crystallinity of g-C_3N_4 was examined using a D8 ADVANCE (Bruker AXS GMBH, Germany) with a scan rate of 4° min^{-1}, a range of 4-45°, and a Cu K_α radiation power of 2.2 kW. Chemical bonds in g-C_3N_4 were analyzed using an FT-IR NEXUS (Thermo Fisher Nicolet, USA). X-ray photoelectron spectroscopy measurements were performed with an AXIS Supra by Kratos Analytical Inc. using monochromatized Al K_a radiation ($h\nu = 1486.6$ eV, 150 W) as the X-ray source, with a base pressure of 10^{-9} torr. Survey scan spectra were acquired with a pass energy of 160 eV and a 1 eV step size. Narrow region scans were obtained with a pass energy of 40 eV and a 0.1 eV step size. The hybrid lens mode was used in both cases. The analyzed area of all XPS spectra was 300 × 700 μm^2. A charge neutralizer was used throughout since the samples were mounted to be electrically isolated from the sample bar. All spectra were calibrated to C 1 s (284.8 eV).

2.5. Photochemical regeneration of $NCBs_{red}$

Photochemical regenerations of $NCBs_{red}$ and NADH were conducted

using a photocatalytic instrument (Shanghai 3S Technology Co., Ltd. SSSTECH-AL1 BV 1.0). The reaction mixture was prepared by dissolving g-C_3N_4, cofactor, and Cp*Rh(bpy)H_2O^{2+} in a TEOA solution at pH 7.5. Light source is a blue light lamp (wavelength: 460 ± 5 nm). The concentration of the reduced cofactor was monitored by measuring the absorbance change of the reaction solution at the characteristic absorption peaks of NADH and $NCBs_{red}$. The absorption peaks (and molar extinction coefficient) of NADH, BANAH [21], BNAH [20], P2NAH [17], P3NAH [17] are 340 nm (6220 M^{-1} cm^{-1}), 360 nm (2200 M^{-1} cm^{-1}), 360 nm (7400 M^{-1} cm^{-1}), 360 nm (3900 M^{-1} cm^{-1}), and 360 nm (8300 M^{-1} cm^{-1}), respectively. The yield, $TOF_{g\text{-}C_3N_4}$, $TTN_{g\text{-}C_3N_4}$ (due to the yellowing of the reaction system after 40 min, TTN was calculated from the first 40 min of the reaction) of the reduced cofactor were calculated according to the following equations:

$$Yield\,(\%) = \frac{(Concentration\ of\ NCBs_{red}\ at\ a\ given\ time)}{(Initial\ concentration\ of\ NCBs_{ox})} \times 100$$

$$TOF_{g-C_3N_4}\left(mmol\ g^{-1}\ h^{-1}\right) = \frac{(Concentration\ of\ NCBs_{red}\ at\ the\ given\ time)}{(Concentration\ of\ g-C_3N_4 \times\ time)}$$

$$TTN_{g-C_3N_4}\left(mmol\ g^{-1}\right) = \frac{(Maximum\ concentration\ of\ NCBs_{red})}{(Concentration\ of\ g-C_3N_4)}$$

2.6. Electrochemical characterization

Voltammetric analyses were conducted using a single-cell compartment in a three-electrode configuration connected to a potentiostat/galvanostat (WMPG 1000, Wonatech Co, Korea). The electrode system in all cyclic voltammetry spectra measurements consisted of a glassy carbon disk electrode (working electrode, radius: 1.5 mm), Ag/AgCl (3 M NaCl) electrode (reference electrode), and Pt wire (counter electrode). Electrochemical analysis was performed at a scanning rate of 50 mV s^{-1}, within a scanning range of −1.0 to 0 V. Six scans were conducted. In the 5th and 6th cycles, the measurement system tended to stabilize and the measurement curve closed. The redox potential was calculated based on the reversible peaks of the 5th and 6th cycles. The working electrode used for transient photocurrent response measurements was a gold electrode. Prior to use, the gold electrode was immersed in a piranha solution (a mixture of 2.8 mL concentrated sulfuric acid and 1.2 mL 30 % hydrogen peroxide solution) for 30 min. Subsequently, it was polished with alumina powder until smooth. After treatment, a suspension of 20 mg mL^{-1} g-C_3N_4 was dropped onto the gold electrode head, left to air dry, and then 5 % Nafion solution was added and air-dried again. During testing, the initial voltage was set to 0.5 V, sensitivity (A/V) was set to 1 e^{-7} V, and blue light with a wavelength of 460 ± 5 nm was used as the light source, with the light source switched every 3.5 s.

2.7. Preparation of XenA

XenA was expressed in *Escherichia coli* BL21 (DE3) strain carrying the pET28a plasmid for XenA expression (the plasmid was preserved in our laboratory). A single colony of BL21 (DE3)/pET28a/XenA was selected from a kanamycin-resistant plate and inoculated into 10 mL LB medium containing kanamycin (100 μg mL^{-1}) for an overnight culture. A 1 % inoculum was transferred to 700 mL LB medium with kanamycin and grown at 37 °C until the OD_{600} of the culture reached approximately 1.5. IPTG was added to a final concentration of 0.1 mM, and induction was performed at 16 °C for 20 h. Cells were harvested by centrifugation at 4 °C, 8000 rpm for 5 min, and the cell pellet was collected after removing the fermentation supernatant. The cell pellet was resuspended in 100 mM HEPES buffer (pH 7.4), sonicated, and XenA protein was eluted by washing with HEPES buffer containing 200 mM imidazole. The eluted XenA protein was collected, desalted, and concentrated. XenA protein expression was confirmed by SDS-PAGE.

2.8. Photocatalytic artificial cofactor coupling XenA

The XenA-driven biocatalytic reduction was coupled with the photochemical regeneration of $NCBs_{red}$. The reaction mixture included g-C_3N_4, $NCBs_{ox}$ (or NAD^+), Cp*Rh(bpy)H_2O^{2+}, XenA, and the substrate 4-Ketoisophorone in a HEPES buffer (100 mM, pH 7.5). Reactions were carried out under illumination (Light source: a 10 W blue lamp with a wavelength of 460 ± 5 nm) in a photocatalytic instrument at 30 °C. For quantitative product analysis, extract the reaction system with twice the volume of ethyl acetate, collect the supernatant, remove remaining water with anhydrous sodium sulfate. Data were analyzed by GC with a flame ionization detector (FID) using a CP-Chirasil-Dex CB column (#CP7502, Agilent, 25 m × 0.32 mm × 0.25 μm); 250 °C injection, split ratio: 50, linear velocity: 25.4 cm s^{-1}. Temperature program: 80 °C hold 2 min; 5 °C min^{-1} to 90 °C hold 2 min; 5 °C min^{-1} to 100 °C hold 2 min; 5 °C min^{-1} to 110 °C hold 2 min; 5 °C min^{-1} to 120 °C hold 2 min; 40 °C min^{-1} to 200 °C hold 2 min. The yields were calculated according to the following equations:

$$Yield(\%) = \frac{(Concentration\ of\ product\ at\ a\ given\ time)}{(Initial\ concentration\ of\ substrate)} \times 100$$

$$TOF_{XenA}\left(h^{-1}\right) = \frac{(Concentration\ of\ levodione\ at\ the\ given\ time)}{(Concentration\ of\ XenA\ \times\ time)}$$

$$TTN_{XenA}\left(mmol\ mg^{-1}\right) = \frac{(Maximum\ concentration\ of\ levodione)}{(Concentration\ of\ XenA)}$$

3. Results and discussion

3.1. Synthesis and characterization of photocatalyst g-C_3N_4

Referring to reported synthesis method for g-C_3N_4 [20], urea was subjected to high-temperature calcination to obtain product as light yellow powder shown in Fig. S1. Subsequently, various analytical methods were used to characterize the synthesized material.

The results of cold field emission scanning electron microscopy (FE-SEM) were depicted in Fig. 1a, revealing a loose layered structure in the synthesized material. Transmission electron microscopy (TEM) results were shown in Fig. 1b, confirming the layered morphology and disclosing significant porous structures. This morphology was consistent with previous reports [20]. The observed phenomenon could be attributed to the thermal decomposition of urea during heat treatment, leading to the substantial release of NH_3 and CO_2 gases. The loose and porous characteristics of the synthesized material were formed by the abundant gas generated. The substantial gas generation and escape during the reaction was further substantiated by the significant mass loss of the remaining solid substance after heat treatment in crucible.

In addition to morphology observation by FE-SEM and TEM, various analytical methods were employed to analyze the chemical composition and structure of the synthesized material. Raman spectroscopy identified peaks corresponding to tris-triazine ring (C_3N_4) and 3-s-triazine ring (C_6N_7) of g-C_3N_4 (Fig. S2). The powder X-ray diffraction (XRD) indicated consistent crystal plane and in-plane stacking structures of g-C_3N_4 (Fig. S3) [22]. The Fourier-transform infrared (FTIR) spectroscopy (Fig. S4) exhibited consistency with the structure of g-C_3N_4, including stretching vibrations of C—N heterocycles, heptazine rings, triazine units and other structural features [23]. These results suggest that the synthesized material shares similar structural characteristics with g-C_3N_4.

Utilizing X-ray photoelectron spectroscopy (XPS) as illustrated in Fig. S5a–c, the surface chemical composition of the synthesized material was further characterized. Fig. S5a presents the measured XPS spectrum, revealing that the material predominantly consists of C and N elements. In Fig. S5b, the spectrum of C 1s exhibits two peaks: one at 281.9 eV corresponding to sp2 C—C bonds, and the other at 285.1 eV associated

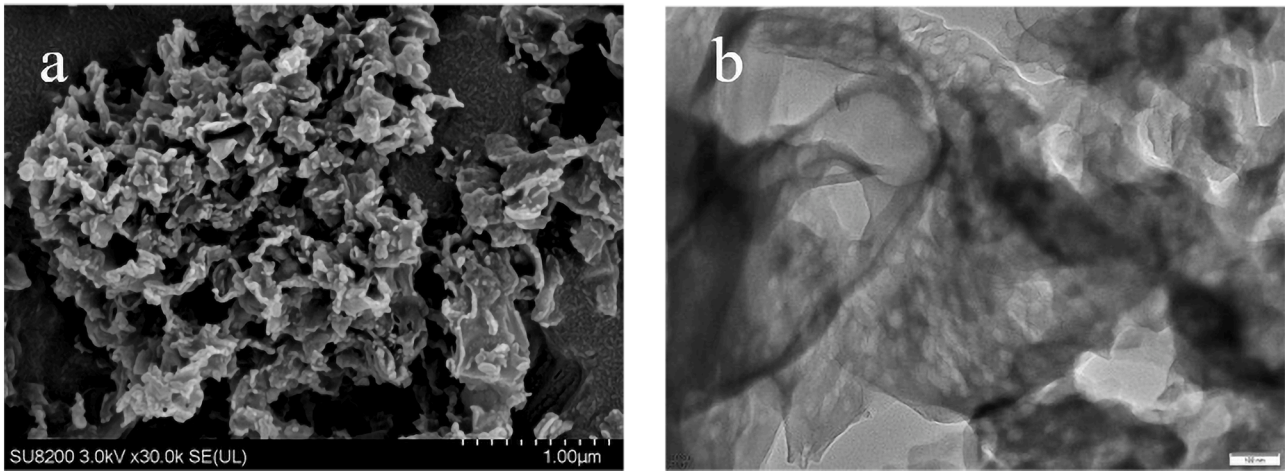

Fig. 1. Cold field emission scanning electron microscopy (FE-SEM) and transmission electron microscopy (TEM) images of the synthesized material. (a) FE-SEM image at 1.0 μm, (b) TEM image at 100 nm.

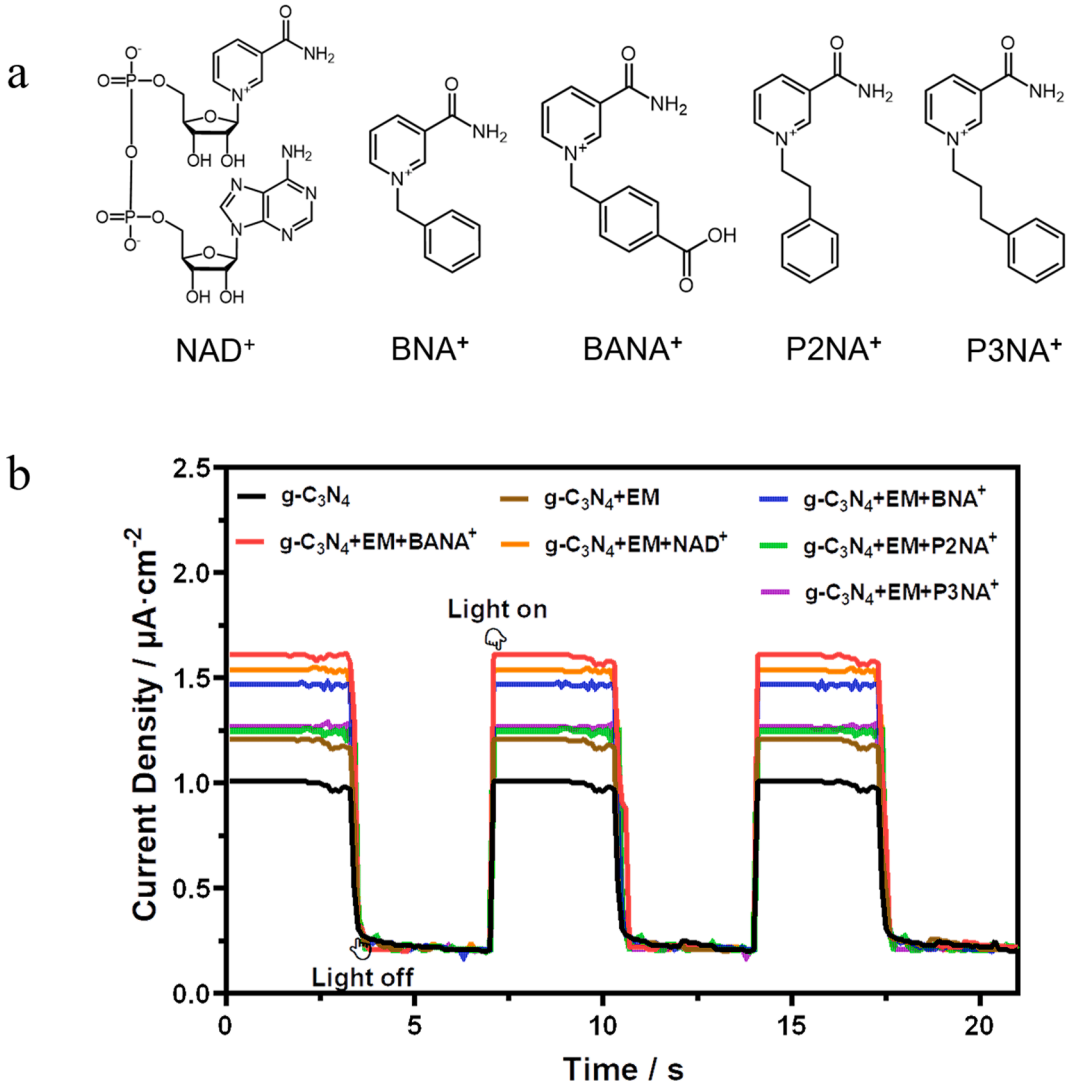

Fig. 2. (a) Chemical structures of NAD^+ and four $NCBs_{ox}$. (b) Transient response of the photocurrent density of g-C_3N_4 with addition of NAD^+ or $NCBs_{ox}$. The working electrode used was a gold electrode coated with g-C_3N_4 and 5 % Nafion. Electrode Ag/AgCl at −0.50 V was used as reference. A blue lamp with a wavelength of 460 ± 5 nm was employed. The reaction was performed with 50 μM EM and 50 μM NAD^+ or $NCBs_{ox}$ in PBS (50 mM, pH 7.5). (For interpretation of the references to colour in this figure legend, the reader is referred to the web version of this article.)

with sp2-hybridized carbon in the nitrogen-containing aromatic ring (N-C═N). The spectrum of N 1 s presented two typical peaks, along with an additional peak and a diminished signal (Fig. S5c). The larger peak was attributed to sp2-hybridized aromatic nitrogen atoms (C-N═C) bound to carbon atoms, while the smaller peak is associated with tertiary N-(C) 3 groups. The ratio of C: N: O, determined from XPS spectrum data, was 0.744:1:0.047 for this material. The discrepancy was presumably due to the significant release of CO_2 during the synthesis process. The theoretical ratio of C: N in g-C_3N_4 should be 0.75:1. The detected oxygen element was attributed to the incomplete isolation of the sample surface from air during synthesis, leading to the adsorption of CO_2 or H_2O. Above characterization results confirmed the success synthesis of g-C_3N_4, which was subsequently used for photochemical experiments.

3.2. Photoelectrochemical properties of photocatalytic g-C_3N_4

The photocatalytic activity of the material depends not only on its light absorption capability but also on the separation and transfer efficiency of photo-generated electron-hole pairs within it. According to previous reports, g-C_3N_4 has a bandgap of 2.7 eV, with corresponding conduction band (CB) and valence band (VB) levels at approximately −1.3 eV and + 1.4 eV, relative to Ag/AgCl reference electrode [24]. This bandgap energy indicates that photoactivated g-C_3N_4 possesses the thermodynamic driving force to reduce EM (with an oxidation–reduction potential of 0.76 V relative to Ag/AgCl [3]).

To confirm the transfer of photoexcited electrons from g-C_3N_4 to EM and subsequently to oxidative cofactor, the transient photocurrent responses of g-C_3N_4 were measured under blue light in various conditions. Artificial cofactors including 1-benzyl-3-carbamoylpyridin-1-ium (BNA^+), 3-carbamoyl-1-(4-carboxybenzyl) pyridin-1-ium ($BANA^+$), 3-carbamoyl-1-phenethylpyridin1-ium ($P2NA^+$), and 3-carbamoyl-1-(3-phenylpropyl) pyridin-1-ium ($P3NA^+$) were synthesized and tested. All of them retained the nicotinamide ring to preserve the biological function of nicotinamide cofactors [17]. Among them, the structure of BNA^+ is the simplest, retaining the nicotinamide ring and a simple benzyl. Other NCBs also feature simple benzyl groups with different substituents, including phenethyl ($P2NA^+$), phenpropyl ($P3NA^+$), and *p*-methylbenzoic acid ($BANA^+$). Considering that the natural cofactors utilized by enzymes are classical 1, 4-NAD(P)H, 1, 4-NCBs were selected to maintain the reactivity and consistence with natural cofactors NCBs. The structures of all four $NCBs_{ox}$ and NAD^+ are shown in Fig. 2a.

As depicted in Fig. 2b, the generation and disappearance of photocurrent were monitored by ON/OFF of blue light. In control group with g-C_3N_4, the separation and transfer of hole-electron pairs in g-C_3N_4 was observed under light conditions. Compared with g-C_3N_4 group, the photocurrent significantly increased from 1.0 μA cm^{-2} to 1.21 μA cm^{-2} after addition of EM to the electrolyte solution. This signifies an improved separation and transfer efficiency of photo-generated electron-hole pairs within the material. Specifically, the photoexcited electrons generated from g-C_3N_4 under light excitation are effectively transferred, facilitating further separation of photo-generated electron-hole pairs and higher photocurrent. Furthermore, varying degrees of increased photocurrent responses were observed when oxidative cofactor was introduced, suggesting continuous transfer of photoexcited electrons from g-C_3N_4 to oxidative cofactor under light irradiation. Among all the experimental groups, the group with $BANA^+$ exhibited the maximum increase in photocurrent, rising from 1.21 μA cm^{-2} to 1.61 μA cm^{-2}. This indicates that the efficiency of photoexcited electron transfer from g-C_3N_4 to $BANA^+$ ranks the highest among four $NCBs_{ox}$ and NAD^+.

The generation of photocurrent with g-C_3N_4, along with the enhancement in photocurrent intensity with the addition of oxidative cofactor, suggests that natural and biomimetic cofactors could be successfully reduced through g-C_3N_4-mediated photocatalytic reactions. In further study, photocatalytic regeneration of various oxidative cofactors was attempted and evaluated.

3.3. Photocatalytic regeneration of NCBs

Based on above photo-electrochemical results, light-driven regeneration of NAD^+ and above four $NCBs_{ox}$ was attempted, including BNA^+, $BANA^+$, $P2NA^+$, and $P3NA^+$. Using g-C_3N_4 as photocatalyst, regeneration of various cofactors to their corresponding reductive forms was performed with blue light illumination in the presence of EM and TEOA.

Detailed parameters of light-driven cofactor regeneration, including total turnover number (TTN) and turnover frequency (TOF) of g-C_3N_4, as well as regeneration yield of NAD^+ and $NCBs_{ox}$, were calculated and summarized in Table 1. Regarding the overall generation yields of various cofactors, the highest yield of 48.32 % was observed with BANAH, followed by NADH (41.66 %), BNAH (37.08 %), P2NAH (6.52 %), and P3NAH (3.12 %). This was basically consistent with above observed highest electron transfer efficiency from g-C_3N_4 to $BANA^+$ as determined by photocurrent responses. The yields of other cofactors also correspond to their profile of photocurrent intensity (Fig. 2b). Similar to the yield, $BANA^+$ group exhibited the highest $TTN_{g\text{-}C_3N_4}$ values after 40 min of reaction. Likewise, $TTN_{g\text{-}C3N4}$ values of other cofactors follow the same ranking as the yield. This indicates that, among all the cofactors, $BANA^+$ features the best performance during the photocatalytic reaction, leading to the highest $TTN_{g\text{-}C3N4}$. With regard to $TOF_{g\text{-}C3N4}$, $BANA^+$ also exhibited excellent regeneration frequency in the first 5 min compared with other artificial cofactors, while lower than that of NAD^+, indicating that NAD^+ had a faster regeneration rate in the initial stage of the reaction. Overall, in contrast to natural cofactor NAD^+, $BANA^+$ exhibited a slower initial regeneration rate, whereas superior reaction stability, with a higher yield. Additionally, since the regeneration efficiencies of both $P3NA^+$ and $P2NA^+$ are relatively low, the slight discrepancy between the photocurrent density (Fig. 2b) and the regeneration yield (Table 1) is resulted from their distinct analytic methods and sampling deviations.

3.4. Cyclic voltammetric analysis of NAD^+ and $NCBs_{ox}$

To elucidate the mechanism responsible for the different regenerative efficiency of cofactors in the photocatalytic system, the distinct catalytic activity of EM towards each cofactor was examined through cyclic voltammetric analysis. The contribution of EM in cofactor reduction was estimated by measuring the increase in the reduction peak current of EM ($I_{EM,\ p}$). According to Fig. 3a and Fig. S6, the $\Delta I_{EM,\ p}$ values follow the order of $BANA^+ > NAD^+ > BNA^+ > P2NA^+ > P3NA^+$. From a thermodynamic point of view, the above ranking of $\Delta I_{EM,\ p}$ could be attributed to the same ranking of their reduction peak potentials ($E_{cofactor,\ p}$) (Fig. 3b and Fig. S6), since the driving force of EM toward reduction of a cofactor becomes higher with a lower $E_{cofactor,\ p}$ values.

Based on their molecular structure, nicotinamide-based cofactors (i.e., NAD^+, BNA^+, $BANA^+$, $P2NA^+$, $P3NA^+$) share a common amide functionality on the C3 atom, which is known for coordinating to the Rh metal center of EM. According to previous report, different substituents of cofactor analogues on the N1 atom exhibit different electron-

Table 1
Performance of light-driven regeneration of NAD^+ and $NCBs_{ox}$ to their reductive forms.

Regenerated cofactor	$TTN_{g\text{-}C3N4}$ [a] [mmol·g^{-1}]	$TOF_{g\text{-}C3N4}$ [b] [mmol·$g^{-1}h^{-1}$]	Yield [a] [%]
NADH	4.12	15.76	41.66
BNAH	3.70	1.46	37.08
BANAH	4.84	8.86	48.32
P2NAH	0.62	0.62	6.52
P3NAH	0.31	0.79	3.12

Determined by UV–Vis spectroscopic analysis after [a] 40 min and [b] 5 min of reaction under blue light illumination. Reactions were performed with g-C_3N_4 (0.20 mg mL^{-1}), EM (100 μM), various cofactors (5 mM) in TEOA solution (500 mM, pH 7.5).

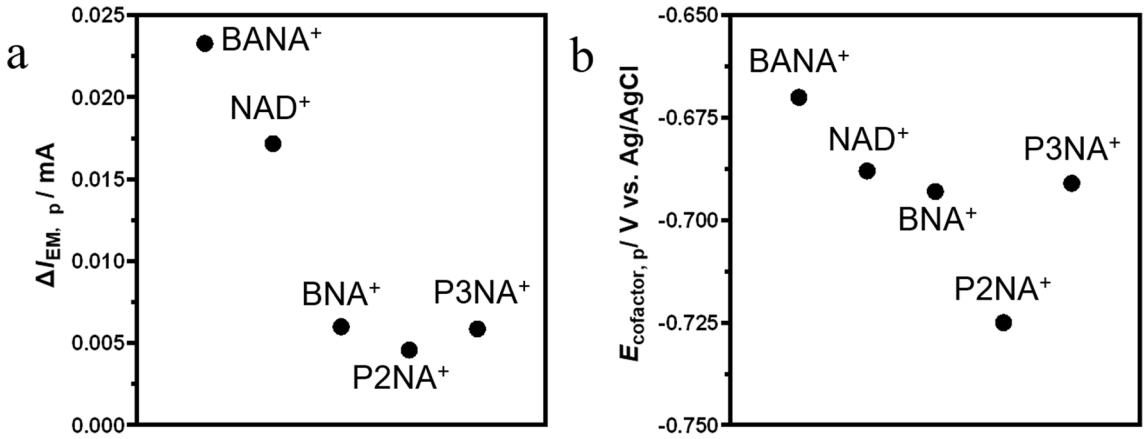

Fig. 3. (a) Comparison of changes in cathodic peak current of 400 μM EM ($\Delta I_{EM,\ p}$) in the presence of 200 μM cofactor. (b) Comparison of reduction peak potentials of cofactors ($E_{cofactor,\ p}$). The electrochemical analysis was carried out in PBS (100 mM, pH 7.5) at a scan rate of 50 mV s^{-1}. Working electrode: a polished glassy carbon electrode.

withdrawing abilities in the order of ribosyl (of NAD^+) > 1-benzyl (of BNA^+) [25], rendering the pyridine ring of BNA^+ less electrophilic. With the elongation of carbon chain between the benzene ring and N1 atom, the electron-donating capacity of the corresponding cofactor become gradually reduced. Specifically, it can be manifested as BNA^+ > $P2NA^+$ > $P3NA^+$. In addition, $BANA^+$ features a negatively charged carboxyl group (at pH 7.5) on the benzene ring. This carboxyl group can interact ionically with the metal center of EM to provide a stronger electron-withdrawing ability endowing $BANA^+$ a superior $E_{cofactor,\ p}$ value than NAD^+. The different $E_{cofactor,\ p}$ values explain the distinct catalytic efficiency of different artificial cofactors and NAD^+ in photocatalytic system. This result also provide inspiration on the design of novel NCBs with higher reduction efficiency. NCBs with superior $E_{cofactor,\ p}$ values could be developed by introducing substituents with stronger electron-withdrawing ability, such as nitrobenzyl, cyanobenzyl etc.

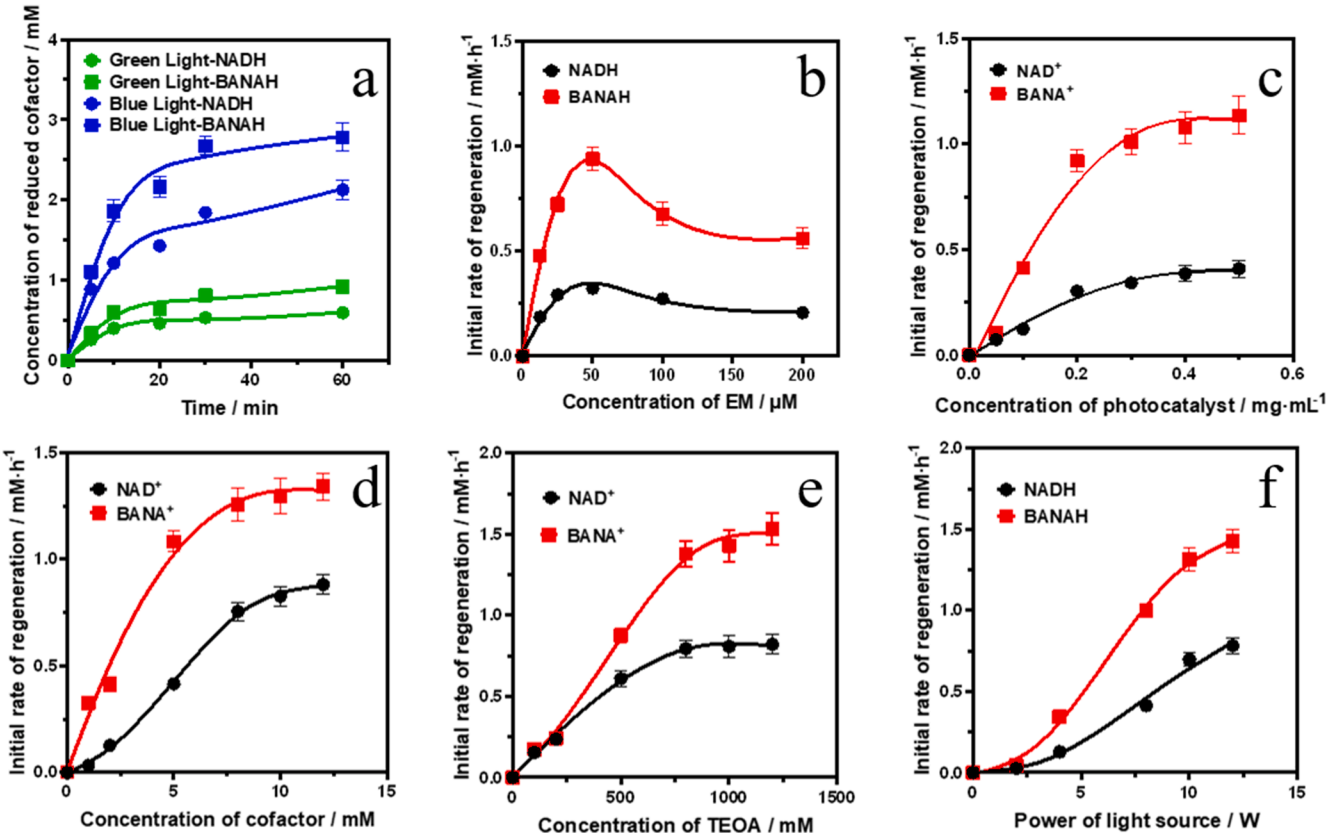

Fig. 4. Effects of (a): wavelengths of light, concentrations of (b) EM, (c) photocatalyst, (d) cofactor, (e) TEOA, and (f) light intensity on the initial regeneration rate. The initial regeneration rate was determined after 10 min of reaction. Reaction conditions: 0–200 μM EM, 0–0.5 mg mL^{-1} g-C_3N_4, 0–12 mM cofactor, 0–1200 mM pH 7.5 TEOA solution, power of light. Source: 0-12 W, wavelength of light: 460 ± 5 nm (blue), 530 ± 5 nm (green). Each reaction condition was optimized based on the previous one. Initial reaction conditions: 100 μM EM, 0.5 mg mL^{-1} g-C_3N_4, 5 mM cofactor, 500 mM pH 7.5 TEOA solution, power of light source: 12 W. (For interpretation of the references to colour in this figure legend, the reader is referred to the web version of this article.)

3.5. Optimization of photocatalytic system

Following above validation, the impact of reaction conditions on photocatalytic cofactor regeneration was investigated. Initially, blue and green lights were selected as light sources to test the effect of light wavelength on the regeneration of reduced coenzyme (Fig. 4a). Additionally, the effects of concentrations of EM, g-C_3N_4, TEOA, and various cofactors, as well as light intensity on the initial cofactor regeneration rate were determined as illustrated in Fig. 4b–f.

Along with natural cofactor NAD^+, $BANA^+$ exhibiting the best performance among $NCBs_{ox}$ was selected to assess the impact of photocatalytic conditions on cofactor regeneration efficiency. It was observed that under blue light conditions, both NAD^+ and $BANA^+$ exhibited superior performance compared with that of green light conditions (Fig. 4a). Under blue light conditions, the concentrations of BANAH and NADH reached 2.78 mM and 2.13 mM after 60 min of reaction. However, under green light, only 0.92 mM and 0.60 mM were attained. This phenomenon can be attributed to the shorter wavelength of blue light, which possesses higher energy and is more efficient in generating photoexcited electron to trigger the reduction reaction. Although the theoretical maximum concentration of 5 mM was not achieved, this might be attributed to suboptimal conditions for each component in the reaction. At various concentrations of g-C_3N_4, TEOA and cofactors, the overall reaction profiles were similar (Fig. 4c–e). At low concentrations of each component, there was a noticeable linear increase in initial reaction rates. While no significant change in initial reaction rate was observed at 0.3 mg mL^{-1} g-C_3N_4, 800 mM TEOA, 8 mM cofactor and above. This could be explained by the fact that under above concentrations, these individual component reached saturation in the system.

Unlike above, for EM, the reaction displayed the highest initial reaction rate at 50 μM, and the initial reaction rate began to decline beyond this concentration (Fig. 4b). This observation suggests that higher concentrations of EM might engage in a reverse reaction involving oxidation of the cofactor, leading to reduced efficiency of photocatalytic process. Furthermore, the increased power of light source also led to an enhancement in initial reaction rate (Fig. 4f). And the highest initial regeneration rate of 1.43 mM h^{-1} with $BANA^+$ was achieved at 12 W. However, beyond a light source power of 10 W, the increase in the initial reaction rate diminished. Due to the limitation of photocatalytic instrument, performance at light power beyond 12 W was not evaluated.

3.6. Oye-catalyzed reduction coupled with photocatalytic regeneration of $NCBs_{ox}$

Based on optimized photocatalytic system, the photocatalytic cofactor regeneration was coupled with biocatalytic reduction by XenA, which has been proven to utilize NCBs as cofactors [26]. 4-Ketoisophorone was selected as the model substrate of XenA, and the product levodione is a key intermediate for carotenoid synthesis [21]. Also, the XenA-catalyzed reduction of 4-Ketoisophorone features a low K_m value and high conversion. As shown in Fig. 5a, the reduced cofactor was consumed during the process of XenA catalyzed reduction of 4-Ketoisophorone to levodione. The photocatalytic system was coupled with this process to confirm that there is no interference between the photocatalytic cofactor regeneration system and enzyme catalytic reaction.

The highest initial reaction rate was observed when $BANA^+$ was employed as the cofactor, leading to a complete conversion of 4-Ketoisophrone to levodione within 180 min. The corresponding GC results are illustrated in Figs. S7–S8. When NAD^+ was utilized, similar initial reaction rate was observed. However, the increase in conversion ratio significantly decelerated after 60 min, resulting in a final conversion ratio of only 77 %. Here, $BANA^+$ demonstrates the application potential of nicotinamide coenzyme biomimetic as "better than nature". NCBs of BNA^+, $P2NA^+$, and $P3NA^+$ were also incorporated into the light-enzyme coupling system. The final conversion ratios in the reaction with $P2NA^+$

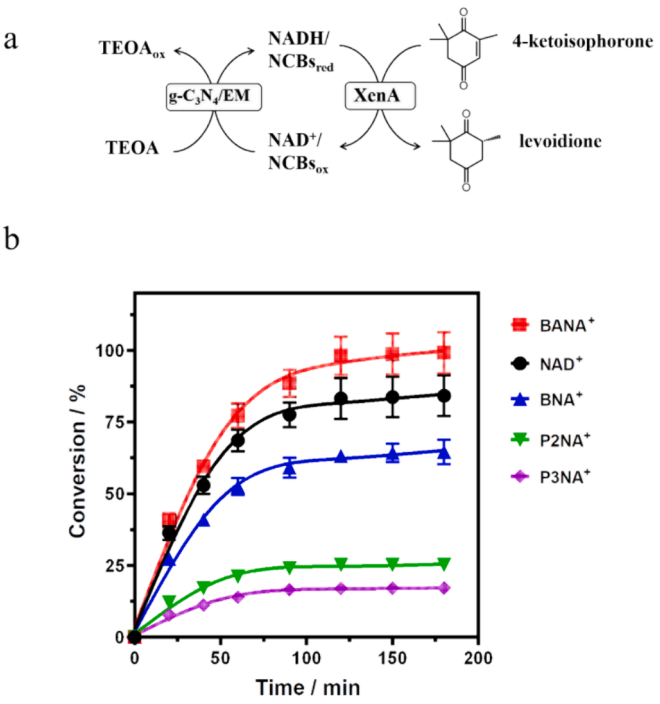

Fig. 5. (a): XenA-catalyzed reduction coupled with photocatalytic regeneration of $NCBs_{ox}$. (b): Time course of enzymatic reduction of 4-Ketoisophorone coupled with photochemical regeneration of various cofactors. Reaction conditions: 0.30 mg mL^{-1} g-C_3N_4, 50 μM EM, 8 mM oxidative cofactor, 0.05 mg mL^{-1} XenA, 10 mM 4-Ketoisophorone, 800 mM TEOA, and 100 mM pH 7.5 HEPES buffer at 30 ℃ in a photocatalytic instrument. Light intensity: 10 W, light. Source: blue lamp. (For interpretation of the references to colour in this figure legend, the reader is referred to the web version of this article.)

and $P3NA^+$ as cofactor were below 25 %, while BNA^+ displayed a moderate level. It can be inferred that the conversion ratio (Fig. 5b) in different experimental groups is positively correlated with the light-driven regeneration rate of cofactors (Table 1). This suggests that the efficiency of light-excited electron transfer significantly influences the conversion effect of the coupling system.

To verify the stability and reusability of the photocatalyst, recycling of g-C_3N_4 in photo-enzymatic coupled reaction was conducted with $BANA^+$ and NAD^+ as cofactors, and g-C_3N_4 was separated by centrifugation for the next cycle of reaction. As shown in Fig. 6a, the conversion ratio of the group with $BANA^+$ in the first reaction was taken as 100 %, and the relative conversion ratio of NAD^+ was calculated to be 89.6 %. After eight cycles of reaction, the relative conversion ratio of the group using $BANA^+$ remained at 93.6 %, representing a decrease of merely 6.4 %. And the conversion ratio after each cycle did not decrease significantly compared with the first cycle. Meanwhile, a similar phenomenon was observed with the group using NAD^+ as a cofactor. After eight recycles, a relative conversion ratio of 82.1 % was determined, which was 7.5 % lower than the first cycle. And no significant difference in conversion ratio was observed after each cycle. The slight decrease in conversion ratio could partially be ascribed to the loss of g-C_3N_4 during recycling process. Furthermore, the separated g-C_3N_4 was characterized by FE-SEM (Fig. 6b) and TEM (Fig. 6c). It was observed that g-C_3N_4 remained structurally stable without significant changes in morphology after eight recycles. Above results demonstrate that g-C_3N_4 features high stability and outstanding reusability as a photocatalyst, and can be recycled in photo-enzymatic reactions while maintaining high conversion ratios.

The effect of initial cofactor concentration on the photo-enzymatic reaction was investigated (Fig. 7). For $BANA^+$, no significant change was observed over 0.05 − 8 mM $BANA^+$, and 100 % conversion was

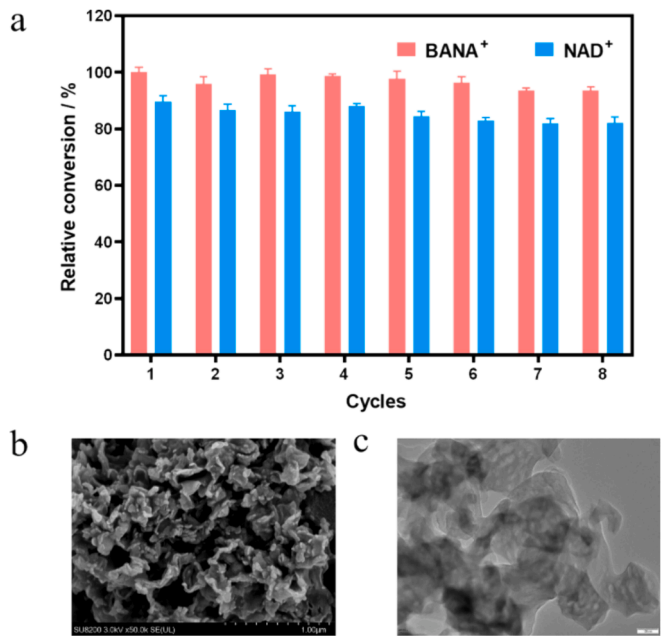

Fig. 6. (a) Recycling of g-C_3N_4 in photo-enzymatic transformation of 4-Ketoisophorone to levodione with $BANA^+$ and NAD^+ as cofactors. Reaction conditions: 0.30 mg mL^{-1} g-C_3N_4, 50 μM EM, 8 mM $BANA^+/NAD^+$, 0.05 mg mL^{-1} XenA, 10 mM 4-Ketoisophorone, 800 mM TEOA, and 100 mM pH 7.5 HEPES buffer at 30 ℃ in a photocatalytic instrument. Light intensity: 10 W, light. Source: blue lamp. Collect g-C_3N_4 through centrifugation, washing, and drying after each reaction for the next cycle reaction. (b) Characterization of g-C_3N_4 after eight cycles by FE-SEM image at 1.0 μm, and (c) TEM image at 100 nm. (For interpretation of the references to colour in this figure legend, the reader is referred to the web version of this article.)

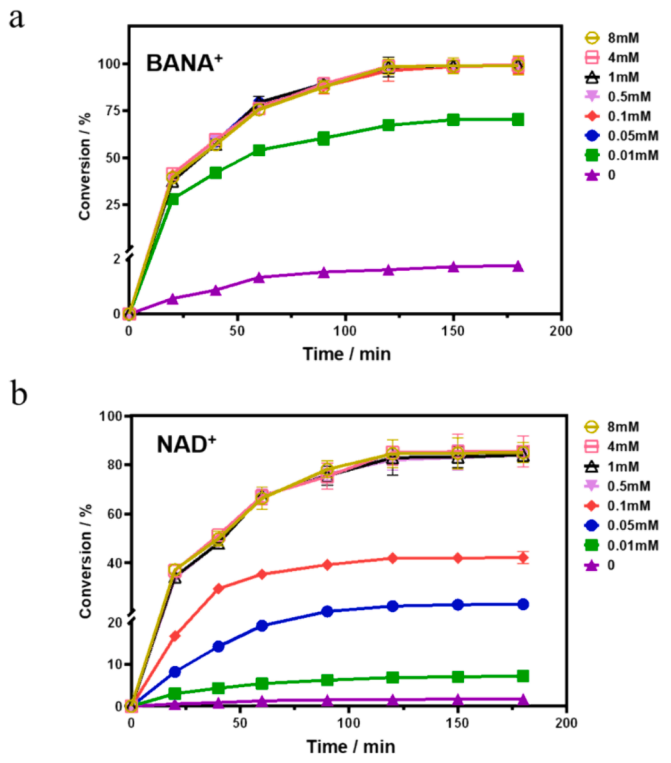

Fig. 7. Effect of different concentrations of cofactors on coupled XenA-catalyzed reduction with photocatalytic system. (a) $BANA^+$. (b) NAD^+. Reaction conditions: 0.30 mg mL^{-1} g-C_3N_4, 50 μM EM, 0–8 mM $BANA^+/NAD^+$, 0.05 mg mL^{-1} XenA, 10 mM 4-Ketoisophorone, 800 mM TEOA, and 100 mM pH 7.5 HEPES buffer at 30 ℃ in a photocatalytic instrument. Light intensity: 10 W, light. Source: blue lamp. (For interpretation of the references to colour in this figure legend, the reader is referred to the web version of this article.)

reached, whereas a compromised conversion of 70.3 % was resulted at a reduced $BANA^+$ of 0.01 mM. In contrast, at least 0.5 mM NAD^+ was required to achieve around 80 % conversion, and the conversion dropped to 42.1 % with 0.1 mM NAD^+. For the control group without cofactors, 1.74 % conversion may be due to the direct transfer of photoexcited electrons to the FMN portion of XenA under illumination conditions [27]. Therefore, the photo-enzyme coupled system requires only 10 % of the initial $BANA^+$ amount compared with NAD^+. The excellent catalytic performance of $BANA^+$ as a cofactor may be attributed not only to its higher reduction efficiency, but also to the higher catalytic efficiency of XenA with $BANA^+$ [21,26].

Here, by coupling g-C_3N_4-mediated photocatalytic cofactor regeneration system, TOF_{XenA} of 322.4 h^{-1} and TTN_{XenA} of 591.2 mmol mg^{-1} were achieved in the overall reaction. In comparison to other photocatalytic systems reported for cofactor regeneration of OYE, the g-C_3N_4-mediated system employed in this study demonstrates outstanding performance with NAD^+ as well as NCBs. As depicted in Table 2, compared with systems using Eosin Y and methyl viologen, in which photoexcited electrons are directly transferred to flavin FMN moiety with no nicotinamide cofactor involved, this study exhibits higher TOF_{XenA} and TTN_{XenA} by utilizing g-C_3N_4 for BANAH regeneration to drive OYE reaction. Our result indicates that OYE-catalyzed reaction could be significantly accelerated by coupling with photocatalytic regeneration of BANAH. This is presumably due to the easier transfer of photoexcited electrons to $BANA^+$ compared with FMN_{OX}. Remarkably, by coupling with photocatalytic system using g-C_3N_4, the yield of levodione exceeded 99 %. This represents the highest efficiency among all photocatalytic coupling systems. Compared with *N*-CDs (*N*-doped carbon nanodots) systems mediated by BNAH, the g-C_3N_4 system exhibited a slower reaction rate. This difference could be ascribed to a broader bandgap of *N*-CDs (2.74 eV, [28] compared to g-C_3N_4 with 2.7 eV), resulting in the formation of photoexcited electron-hole pairs that are more difficult to recombination and easier to transfer. Consequently, modification of photocatalysts based on cofactor structures could be important to adjust its redox potential and achieve higher catalytic efficiency [3]. In addition, the efficiency of photocatalytic systems can also be improved by preparing functionalized porous carbon nitride nanosheets (MFPCN) to increase the specific surface area [29], or constructing heterojunction catalysts to promote electron transfer [30]. Notably, $BANA^+$ demonstrates a superior $E_{cofactor,\ p}$ value than BNA^+ and even NAD^+ (Fig. 3b), indicating substantial potential for advancing the artificial coenzyme $BANA^+$ in the field of photocatalytic regeneration, potentially exceeding its natural counterparts.

4. Conclusions

An efficient photocatalytic cofactor regeneration system was developed for the participation of artificial cofactors in OYE-catalyzed conversion of 4-Ketoisophorone to levodione. Based on spectroscopic and photo-electrochemical analysis, the efficacy of g-C_3N_4 to deliver photoexcited electrons to EM and the distinct photochemical reduction behaviors of NAD^+ and $NCBs_{ox}$ was elucidated. Initial rates and yields of regeneration follow BANAH > NADH > BNAH > P2NAH > P3NAH, which are in line with their reduction peak potentials. By coupling of photochemical regeneration of $NCBs_{red}$ with OYE-driven reaction, successful reduction of 4-Ketoisophorone was achieved. Among all cofactors tested, BANAH excels in levodione production, consistent with its prominent regeneration performance in the photocatalytic system, as well as its high $\Delta I_{EM,\ p}$ and $E_{cofactor,\ p}$ values. Moreover, after multiple recycles in photo-enzymatic reaction, g-C_3N_4 maintained over 93.6 % catalytic efficiency with $BANA^+$. Due to its high stability and reusability, as well as easy preparation, g-C_3N_4 has excellent prospects for practical

Table 2
Comparison of photobiocatalytic efficiencies in this study and reported OYE-catalyzed reduction.

Photocatalyst	Cofactor	OYE	TOF_{XenA} [h^{-1}]	TTN_{XenA} [mmol mg^{-1}]	Yield [%]	Reference
g-C_3N_4	$BANA^+$	XenA	322.4	591.2	>99	This work
N-CDs	BNA^+	*Ts*OYE	576.3	838.9	>99	Park, C.B. [28]
Eosin Y	FMN_{OX}	*Ts*OYE	118.0	295.0	67	Park, C.B. [27]
Methyl viologen	FMN_{OX}	TOYE	121.5	500.0*	>99	Scrutton, N. S. [31]
		PETNR	100.4	445.0*	89	

* Based on the calculation results in reference 28.

applications. In addition, compared with natural cofactor NAD^+, $BANA^+$ has advantages such as higher stability and lower synthesis costs. Due to the high stability of $BANA^+$ regeneration system using g-C_3N_4, it can be applied by combining with enzymes capable of utilizing NCBs, such as salicylate hydroxylase, glucose dehydrogenase [32] etc. Overall, the light-driven approach to regenerate cofactor analogues better than nature is a promising strategy for efficiently driving oxidoreductases-catalyzed reactions using light energy. Additionally, the photocatalytic cofactor regeneration system can also be integrated with photo-enzymatic reaction to inspire the development of novel photo-biocatalysis processes [33–35].

CRediT authorship contribution statement

Feifan Luo: Writing – original draft, Visualization, Validation, Methodology, Investigation, Data curation. **Xiangyuan Gu:** Methodology, Data curation. **Yichun Zhu:** Investigation, Formal analysis. **Jieyu Zhou:** Writing – review & editing, Supervision, Conceptualization. **Guochao Xu:** Methodology, Formal analysis. **Ye Ni:** Writing – review & editing, Supervision, Project administration, Methodology, Funding acquisition, Conceptualization.

Declaration of competing interest

The authors declare that they have no known competing financial interests or personal relationships that could have appeared to influence the work reported in this paper.

Acknowledgements

This work was supported by the National Key R&D Program (2021YFC2102700), Fundamental Research Funds for the Central Universities (JUSRP122038), and the National Natural Science Foundation of China (22377040, 21907040).

Appendix A. Supplementary data

Supplementary data to this article can be found online at https://doi.org/10.1016/j.bioorg.2024.107418.

References

[1] O. Akinterinwa, R. Khankal, P.C. Cirino, Curr. Opin. Biotechnol. 19 (2008) 461–467, https://doi.org/10.1016/j.copbio.2008.08.002.
[2] K. Vedha-Peters, M. Gunawardana, J. Rozzell, S. Novick, J. Am. Chem. Soc. 128 (2006) 10923–10929, https://doi.org/10.1021/ja0603960.
[3] V. Ganesan, D. Sivanesan, S. Yoon, Inorg. Chem. 56 (2017) 1366–1374, https://doi.org/10.1021/acs.inorgchem.6b02474.
[4] X. Wang, H.H.P. Yiu, ACS Catal. 6 (2016) 1880–1886, https://doi.org/10.1021/acscatal.5b02820.
[5] Advances in Biochemical Engineering/biotechnology 120 (2010) 195–242.
[6] M.A. Emmanuel, S.G. Bender, C. Bilodeau, J.M. Carceller, J.S. DeHovitz, H. Fu, Y. Liu, B.T. Nicholls, Y. Ouyang, C.G. Page, T. Qiao, F.C. Raps, D.R. Sorigué, S. Sun, J. Turek-Herman, Y. Ye, A. Rivas-Souchet, J. Cao, T.K. Hyster, Chem. Rev. 123 (2023) 5459–5520, https://doi.org/10.1021/acs.chemrev.2c00767.
[7] D. Vasic-Racki, Industrial Biotransformations, Wiley Press, New Jersey 1 (2006) 1–36.
[8] M. Yuan, M.J. Kummer, R.D. Milton, T. Quah, S.D. Minteer, ACS Catal. 9 (2019) 5486–5495, https://doi.org/10.1021/acscatal.9b00513.
[9] G.T. Höfler, E. Fernández-Fueyo, M. Pesic, S.H. Younes, E.G. Choi, Y.H. Kim, V. B. Urlacher, I.W.C.E. Arends, F. Hollmann, Chembiochem 19 (2018) 2344–2347, https://doi.org/10.1002/cbic.201800530.
[10] Y. Wang, J. Sun, H. Zhang, Z. Zhao, W. Liu, Catal Sci & Technol. 8 (2018) 2578–2587, https://doi.org/10.1039/c8cy00320c.
[11] A. Dhankhar, V. Jain, I.N. Chakraborty, P.P. Pillai, J. Photochem. Photobiol. A Chem. 437 (2023) 114472, https://doi.org/10.1016/j.jphotochem.2022.114472.
[12] R.K. Yadav, A. Kumar, N.J. Park, D. Yadav, J.O. Baeg, ChemCatChem 9 (2017) 3153–3159, https://doi.org/10.1002/cctc.201700789.
[13] J. Meng, Y. Tian, C. Li, X. Lin, Z. Wang, L. Sun, Y. Zhou, J. Li, N. Yang, Y. Zong, F. Li, Y. Cao, H. Song, Cataly Sci & Technol. 9 (2019) 1911–1921, https://doi.org/10.1039/c9cy00180h.
[14] M. M. Grau, M. Poizat, I. W. C. E. Arends, F. Hollmann, Appl Organometal Chem., (2010), 24, 380-385. https://doi.org/ 10.1002/aoc.1623.
[15] Z. Liu, J. Li, Z. Chen, M. Li, L. Wang, S. Wu, J. Zhang, Appl Catal B-Environ. (2023) 326, https://doi.org/10.1016/j.apcatb.2022.122338.
[16] C.E. Paul, D. Tischler, A. Riedel, T. Heine, N. Itoh, F. Hollmann, ACS Catal. 5 (2015) 2961–2965, https://doi.org/10.1021/acscatal.5b00041.
[17] C. Nowak, A. Pick, P. Lommes, V. Sieber, ACS Catal. 7 (2017) 5202–5208, https://doi.org/10.1021/acscatal.7b00721.
[18] M.M.C.H. van Schie, C.E. Paul, I.W.C.E. Arends, F. Hollmann, Chem. Commun. 55 (2019) 1790–1792, https://doi.org/10.1039/c8cc08149b.
[19] B. Zhu, P. Xia, W. Ho, J. Yu, Appl. Surf. Sci. 344 (2015) 188–195, https://doi.org/10.1016/j.apsusc.2015.03.086.
[20] H.C. Lo, R.H. Fish, Angew. Chem. Int. Ed. 41 (2002) 478–481, https://doi.org/10.1002/1521-3773(20020201)41:3<478::AID-ANIE478>3.0.CO;2-K.
[21] N. Falcone, Z. She, J. Syed, A. Lough, H.B. Kraatz, Chembiochem 20 (2019) 838–845, https://doi.org/10.1002/cbic.201800661.
[22] Z. Xing, Z. Ju, Y. Zhao, J. Wan, Y. Zhu, Y. Qiang, Y. Qian, Sci. Rep. 6 (2016) 26146, https://doi.org/10.1038/srep26146.
[23] Q. Lin, L. Li, S. Liang, M. Liu, H.M.J. Bi, L. Wu, Appl. Catal B-Environ. 163 (2015) 135–142, https://doi.org/10.1016/j.apcatb.2014.07.053.
[24] Q. Tan, S.F. Ng, A.R. Mohaned, W.J. Ong, Carbon Energy. 4 (2022) 665–730, https://doi.org/10.1002/cey2.252.
[25] H.C. Lo, O. Buriez, J.B. Kerr, R.H. Fish, Angew. Chem. Int. Ed. 38 (1999) 1429–1432, https://doi.org/10.1002/(SICI)1521-3773(19990517)38:103.0.CO;2-Q.
[26] T. Knaus, C. E. Paul, C. W. Levy, S. de Vries, F. G. Mutti, F. Hollmann, N. S. Scrutton, J Am Chem Soc., (2016), 138, 1033-1039. https://doi.org/ 10.1021/jacs.5b12252.
[27] S.H. Lee, D.S. Choi, M. Pesic, Y.W. Lee, C.E. Paul, F. Hollmann, C.B. Park, Angew. Chem. Int. Ed. 56 (2017) 8681–8685, https://doi.org/10.1002/anie.201702461.
[28] J. Kim, S.H. Lee, F. Tieves, D.S. Choi, F. Hollmann, C.E. Paul, C.B. Park, Angew. Chem. Int. Ed. 57 (2018) 13825–13828, https://doi.org/10.1002/anie.201804409.
[29] K. Wang, H. Wang, Q. Cheng, C. Gao, G. Wang, X. Wu, J. Colloid Interface Sci. 607 (2022) 1061–1070, https://doi.org/10.1016/j.jcis.2021.09.034.
[30] Y. Shang, C. Wang, C. Yan, F. Jing, M. Roostaeinia, Y. Wang, G. Chen, C. Lv, J. Colloid Interface Sci. 634 (2023) 195–208, https://doi.org/10.1016/j.jcis.2022.12.039.
[31] M. K. Peers, H. S. Toogood, D. J. Heyes, D. Mansell, B. J. Coe, N. S. Scrutton, Catal Sci Technol., (2016), 6, 169-177. https://doi.org/ 10.1039/c5cy01642h.
[32] E. King, S. Maxel, H. Li, Scrutton, Curr Opin Biotech. 66 (2020) 217–226, https://doi.org/10.1016/j.copbio.2020.08.005.
[33] Y. Xu, H. Chen, L. Yu, X. Peng, J. Zhang, Z. Xing, Y. Bao, A. Liu, Y. Zhao, C. Tian, Y. Liang, X. Huang, Nature 625 (2024) 74–78, https://doi.org/10.1038/s41586-023-06822-x.
[34] N. Sun, J. Huang, J. Qian, T. Zhou, J. Guo, L. Tang, W. Zhang, Y. Deng, W. Zhao, G. Wu, R. Liao, X. Chen, F. Zhong, Y. Wu, Nature 611 (2022) 715–720, https://doi.org/10.1038/s41586-022-05342-4.
[35] L. Cheng, D. Li, B.K. Mai, Z. Bo, L. Cheng, P. Liu, Y. Yang, Science 381 (2023) 444–451, https://doi.org/10.1126/science.adg2420.